ADVANCED OPTICAL MATERIALS
www.advopticalmat.de

Plasmonic and Photonic Modes in Colloidal CuS Nanocrystals

Kenan Elibol, Fatemeh Davoodi, Urvi Parekh, Masoud Taleb, Stefan Scheel, Marko Burghard, Peter A. van Aken, Christian Klinke, Nahid Talebi,* and Rostyslav Lesyuk**

Copper monosulfide (CuS), also known as covellite, displays exceptional optoelectronic characteristics, exhibiting both plasmonic and photonic absorption in its monolithic nanomaterial form. It is classified as a hybrid metallic-semiconducting material and a natural hyperbolic material with a distinctive crystal structure. Nanostructured CuS has been demonstrated to support localized surface plasmon resonances (LSPR) in the near-infrared spectral range. Here, the phenomenon of near-infrared (NIR) to visible electromagnetic field localization in ultrathin crystalline quasi-2D CuS nanocrystals is revealed. This is achieved by mapping LSPRs in a range of CuS structures using high-resolution electron energy-loss spectroscopy in combination with cathodoluminescence spectroscopy. In addition to LSPRs, a range of photonic modes in the visible and ultraviolet spectral ranges is identified in colloidally defined single-crystalline nanostructures, with numerical simulations providing supporting evidence. Finally, CuS nanocrystals exhibit visible NIR light emission within the range of 600–900 nm when excited by an electron beam. Altogether, these properties make CuS nanocrystals highly suitable for applications in telecommunications, sensing, and nanophotonics.

1. Introduction

A variety of low-dimensional semiconductor nanomaterials exhibit prominent excitonic spectral features at room temperature due to stronger binding energy compared to their bulk counterparts as a consequence of modified environmental screening.[1] Moreover, they exhibit size-dependent and thus tunable properties promoted by electronic quantum confinement, including increased effective band gaps and an enhanced density of states at the band edges due to their low dimensionality, which subsequently results in increased absorption. Additionally, in thin films of such materials, the excitons can strongly interact with photonic modes, leading to the formation of self-hybridized exciton-polaritons.[2–7]

Although various van der Waals materials sustain excitonic responses in the visible range, their plasmonic and photonic

K. Elibol, M. Burghard, P. A. van Aken
Max Planck Institute for Solid State Research
Heisenbergstr. 1, 70569 Stuttgart, Germany
F. Davoodi, M. Taleb, N. Talebi
Institute of Experimental and Applied Physics
Christian Albrechts University
24118 Kiel, Germany
E-mail: talebi@physik.uni-kiel.de
F. Davoodi, M. Taleb, N. Talebi
Kiel Nano
Surface and Interface Science KiNSIS
Christian Albrechts University
24118 Kiel, Germany

The ORCID identification number(s) for the author(s) of this article can be found under https://doi.org/10.1002/adom.202402965

[Correction added on January 10, 2025, after first online publication: the affiliations of the 10th named author has been updated in this version.]

DOI: 10.1002/adom.202402965

U. Parekh, S. Scheel, C. Klinke, R. Lesyuk
Institute of Physics
University of Rostock
Albert-Einstein-Straße 23, 18059 Rostock, Germany
E-mail: rostyslav.lesyuk@uni-rostock.de
C. Klinke
Department of Chemistry
Swansea University–Singleton Park
Swansea SA2 8PP, UK
C. Klinke
Department "Life, Light & Matter"
University of Rostock
Albert-Einstein-Straße 25, 18059 Rostock, Germany
E-mail: christian.klinke@uni-rostock.de
R. Lesyuk
Pidstryhach Institute for applied problems of mechanics and mathematics of NAS of Ukraine
Naukowa str. 3b, Lviv 79060, Ukraine

excitations have not been widely studied. This is due to their rather low carrier mobility and density, which limits the plasma frequency of these materials to the far-infrared range, such as in graphene.[8–11] In contrast, borophene has been theoretically proposed,[12] and recently experimentally reported, to support hyperbolic plasmonic responses in the visible range.[13] In addition to van der Waals and synthesized true 2D materials, quasi-2D materials such as ultrathin layers of several materials also exhibit plasmonic responses. Copper sulfide (CuS) nanocrystals are a prominent example of the latter class as a monolithic material.[14–18] CuS exhibits strong metallic-like properties including superconductivity due to its unique electronic configuration and the presence of delocalized free holes arising from its mixed-valence nature.[19–23] Recently, CuS has been shown to be a material with naturally occurring hyperbolicity in the NIR range due to its highly anisotropic crystal structure.[24] Nanocrystals of CuS exhibit very strong and highly tunable plasmonic bands in the near-infrared (NIR) region below the energy of 1.8 eV (telecom window). Moreover, the crystalline structure of this material leads to a highly anisotropic response, and, as we will show, even thin nanosheets of this material with thicknesses below 10 nm support confined photonic modes in a broad energy range between 1.8 and 4 eV. A recent study has shown that the optical bandgap of CuS can be tuned via pressure modulation.[25] CuS used in the Al/Au/CuS heterostructures also plays a critical role in enhancing high-order harmonic generation through its plasmonic properties.[26]

Many potential applications rely on the high plasmonic activity of copper sulfides in the NIR spectral region between 900 and 2500+ nm.[27,28,16] LSPRs similar to those of noble metals are highly dependent on the size, shape, and surface conditions of the materials and, are therefore highly tunable. In addition, stoichiometry plays an important role: the number of quasi-free holes in $Cu_{2-x}S$ increases with $x = \{0,1\}$, leading to the highest plasmon frequency in the covellite phase with x ranging from 0.97 to 1 in the large family of possible copper sulfide phases. Although various studies simulating the electric field distribution in terms of dipolar, quadrupolar, in-plane, and out-of-plane modes of covellite nanocrystals have been reported,[17,24] experimental evidence is still lacking.

Spatially resolved electron energy loss spectroscopy (EELS) implemented in a transmission electron microscope in the focused scanning mode (STEM), offers the possibility to spectroscopically identify plasmonic absorption and to image the plasmonic and photonic modes with a spatial resolution below the optical diffraction limit down to the nanometer scale.[29,30] A variety of plasmonic resonances of different material systems have been studied by EELS, such as in thin metallic flakes,[31,32] in toroidal modes of oligomer nanocavities,[33,34] in conical tapers,[35,36] and in nanorods.[37,32,38] Cathodoluminescence spectroscopy (CLS) is a complementary method that provides access to radiation modes. Whereas EELS maps the full projected photonic local density of states, CLS is analogous to resolving the radiative local density of states.[39,40] Combining CLS with optical detection schemes, including angle-resolved mapping and polarimetry, can reveal the nature of the near-field excitations, such as whether they are dipolar, quadrupolar, vortex beams, or chiral.[41,42]

Despite the extensive study of excitonic responses, plasmonic and photonic properties in low-dimensional or 2D materials remain relatively underexplored, presenting a missed opportunity in the fields of optoelectronics and photonics. Here we address this gap by focusing on copper monosulfide nanocrystals, which offer both plasmonic and photonic responses, potentially unlocking new applications in these domains. We present a comprehensive study of the plasmonic and photonic modes of CuS nanocrystals measured by EELS and CLS and perform simulations to aid in the interpretation of the experimental data. Our analysis reveals highly confined plasmonic modes in faceted CuS quasi-2D nanostructures as thin as 1.7 to 10 nm. Our investigations resolve deep-subwavelength plasmonic modes with polariton wavelengths as short as 30 nm at photon energies of 1.6 eV, leading to an extremely high local density of states supported by CuS NCs as small as only a few tens of nanometers in diameter. In addition, polarimetry CLS resolves the dipolar nature of the dominant plasmonic modes in small NCs and coherent CL illumination due to plasmonic excitations. Our studies demonstrate the high-quality plasmonic responses of CuS NCs, the shape sensitivity of the plasmonic resonances, and the versatility of our synthesis method to fabricate CuS NCs with predefined shapes.

2. Results and Discussion

2.1. Structural and Optical Properties of CuS NCs

The detailed synthesis method and shape tuning are described elsewhere and are based on the oleylamine-based hot-injection protocol.[43] In the present work, triangular and round nanoprisms (quasi-2D nanocrystals) were used. The morphologies of the structures were characterized by TEM and PXRD. In **Figure 1**a–c, TEM images of differently shaped nanocrystals (NC) are shown along with their corresponding XRD patterns. The disk-like NCs have a lateral dimension of ≈20 nm (standard deviation σ = 2.2 nm), whereas the average edge length of the triangular NCs is ≈34 nm (σ = 3 nm). Due to the face-to-face stacking with the edges facing the electron beam, the average thickness of the triangles can be measured directly and is ≈4.0 nm (σ = 0.4 nm). The hexagonal nanoprisms have identical thicknesses and average edge lengths of 47 nm (σ = 3 nm). Interestingly, the distance between NCs in a stack is ≈1–1.2 nm (estimated from TEM images of edge-standing particles, Figure S1g,h, Supporting Information), which could correspond to different isometric configurations of the oleylamine ligands. According to ref., [44] the cis-isomer predominates in the 70% oleylamine with a fraction of ≈78%. Assuming a lateral arrangement on the NCs surface with a double layer of ligands, a minimum distance of ≈0.7 nm can be expected between NCs, which is slightly less than what is observed in the TEM images. The atomic structure of covellite CuS is examined from its HRTEM image and its corresponding image simulation (Figure 1d,e). The majority of the CuS NCs were aligned along the (001) orientation.

The representative XRD pattern shown in Figure 1f confirms the previous general observations from TEM and HRTEM imaging: thin crystallites show a strong texture effect with distinct stacking. One can observe broadened reflections of the (00*l*) planes which dominate over other crystallographic directions (texture effect due to preferential orientation along the (001) plane). The strongest peak at 2θ = 38.9° corresponds well to the (006) reference plane. At low angles, sharp reflections are

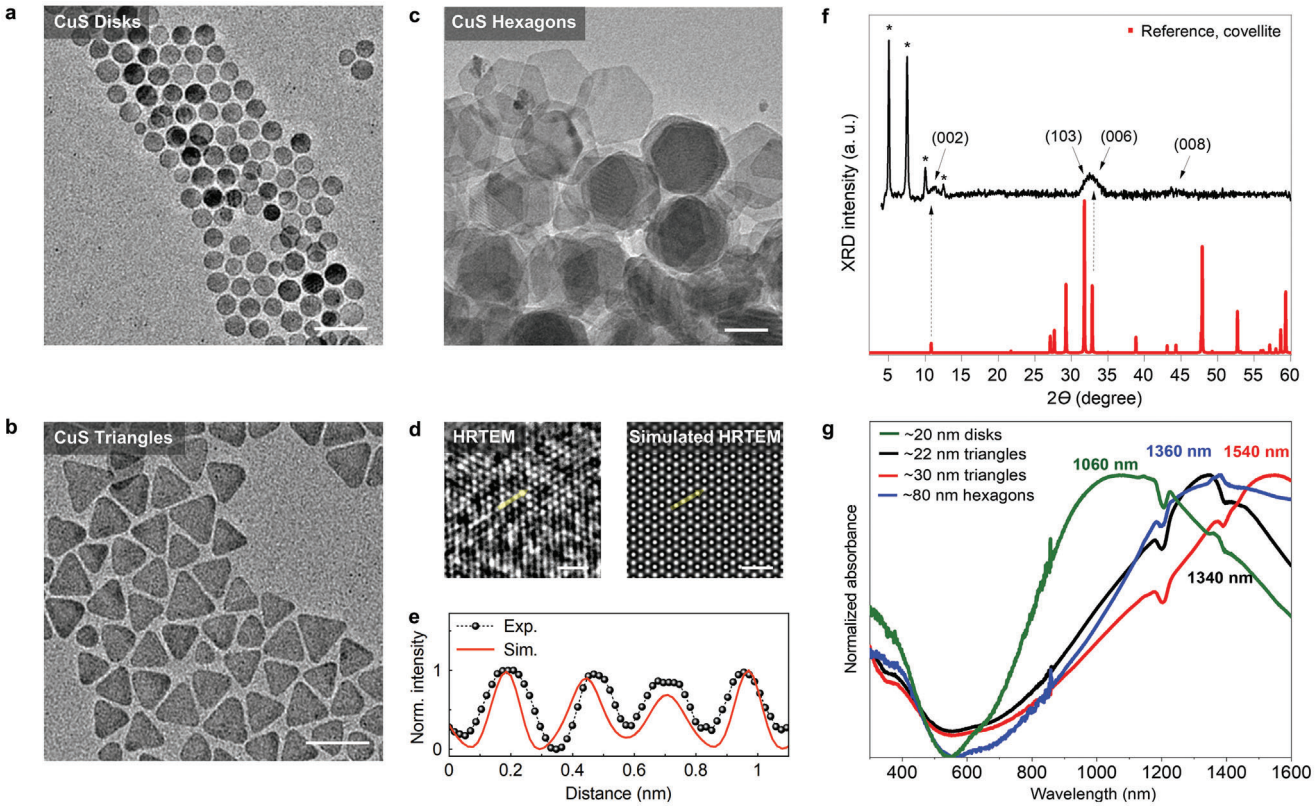

Figure 1. Crystal structure and optical absorption of CuS NCs. a–c) TEM images of colloidal disk, triangular, and hexagonal copper sulfide nanocrystals. d) HRTEM image of a CuS NC and corresponding simulated HRTEM image. e) Line profile recorded along the dashed yellow lines on the experimental and simulated HRTEM images. f) XRD pattern of CuS NCs (triangles) with reference data.[45] The reflections marked with * are due to the periodic structure of stacked NCs. g) Absorption spectra of CuS NCs. Scale bars are 50 nm (a–c) and 1 nm (d).

detected at 5, 7.5, 10, and 12.5°, which are equidistant from each other (marked with *). We attribute these reflections to common *d*-spacing of 35 Å with diffraction order n = 1, 2, 3, 4 in accordance with Bragg's condition arising from the lateral stacking of nanocrystals in the sample on the silicon XRD substrate. The lateral stacking on the substrate obviously differs slightly from the edge stacking in the TEM images, as the peaks correspond to a stacking periodicity of exactly 3.5 nm which in turn corresponds to two crystal units within the CuS nanoprisms. Thus, TEM-based thickness assessment may give a slightly overestimated thickness. The powder XRD pattern of hexagonal NCs is shown in Figure S1 (Supporting Information). The alignment of NCs on the substrate and stacking effect are much less pronounced which can be deduced from vanishing of texture effect and sharp equidistant low-angle reflections.

In Figure 1g, the optical absorption spectra show broad band peaks in the NIR region between 700 and 1800+ nm,–identified as excitation of first-order LSPRs, while the onset of absorption in the visible region below 500 nm, with a shoulder at 390 nm–identified as fundamental absorption.

In order to better identify the characteristics of optical excitations in CuS thin films, we first numerically study the propagating modes supported by thin films. The permittivity of bulk CuS along the in-plane and out-of-plane directions, denoted as $\epsilon_{r,\parallel}$ and $\epsilon_{r,\perp}$, respectively, shows that this material exhibits dielectric behavior above 1.8 eV, while it exhibits metallic behavior below 1.8 eV (**Figure 2a**). Therefore, we expect the excitation of plasmon polaritons in thin films and nanocrystals of CuS at energies below 1.8 eV. Notably, the material also supports guided thin film excitations at energies above 1.8 eV, as shown below, where the latter will be referred to as a photonic mode. The calculated dispersions of photonic and plasmonic modes in 4 and 6.4 nm thick CuS films show that both modes can be supported in thin films (Figure 2b,c). A photonic mode of transverse electric (TE) nature is identified, forming guided waves confined within the boundaries of the thin film and propagating along the z-axis in the energy range of 1.8 to 4.2 eV. At higher energies, the photonic mode has a strongly radiative nature, with its dispersion diagram positioned inside the light cone (Figure 2b). The plasmonic mode, on the other hand, has a transverse magnetic (TM) nature, with its dispersion positioned outside the light cone throughout the energy range below 1.8 eV. For d = 6.4 nm, the ratio of the phase constant of the plasmon polariton waves to the free space wavenumber is between 6 and 40 in the energy range from 1.45 to 1.8 eV. This fact leads to a large confinement of the plasmon polariton waves and to the effective polariton wavelengths being smaller than the free space wavelengths, by the same ratio. Thus, wavelengths as short as 30 nm can be found at a photon energy of 1.6 eV. The 30 nm polariton wavelength in nanoscaled CuS demonstrates extreme spatial confinement, far below the free-space excitation wavelength, enabling enhanced electromagnetic field intensities for nanoscale light-matter interactions, including

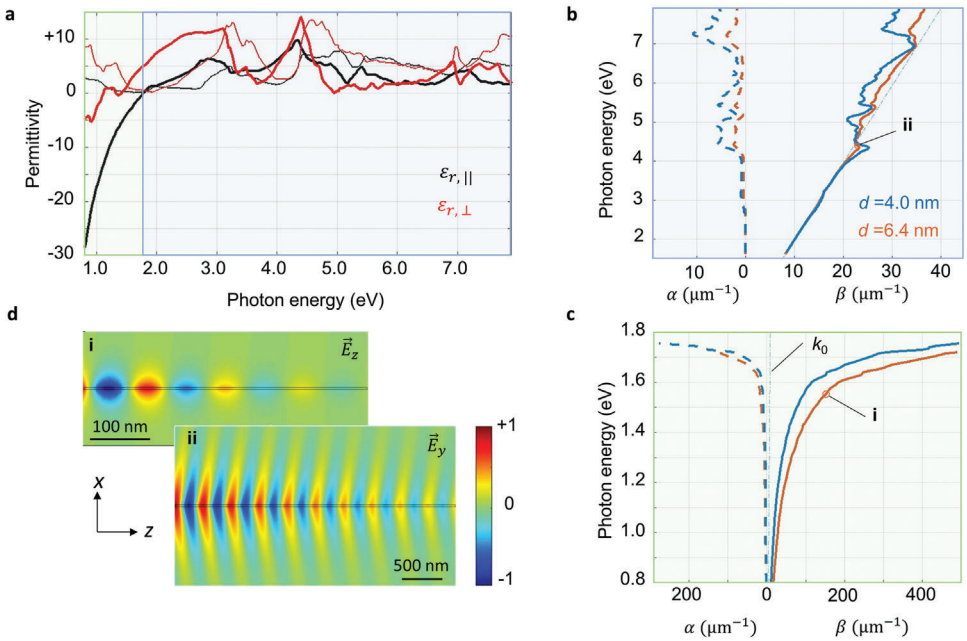

Figure 2. Optical and plasmonic responses of thin CuS films. a) CuS permittivity along the in-plane ($\epsilon_{r,\parallel}$) and out-of-plane ($\epsilon_{r,\perp}$) directions. Solid thick and thin lines show the real part and imaginary parts of the permittivity, respectively. Calculated propagation constants of the $\epsilon_{r,\parallel}\epsilon_{r,\perp}$ b) photonic and c) plasmonic modes propagating along the x-axis for the thin film thicknesses shown. The symmetric configuration is the dominant optical mode. Both the phase constant (β) and the attenuation constant (α) are shown. d) Calculated field profiles of the in-plane electric-field components at two photon energies, associated with (i) plasmonic (E = 1.55 eV) and (ii) photonic modes (E = 4.3 eV), where the former is in the form of TM and the latter is in the form of TE modes.

single-molecule detection, nonlinear optics, and quantum coupling. The electric field profiles tangential to the surface of both the plasmonic and photonic modes in CuS at energies of 1.55 and 4.3 eV, respectively, are shown in Figure 2d. It is noteworthy that the material exhibits a hyperbolic response in the energy range of 1.11 to 1.79 eV, as the in-plane permittivity is negative, while the out-of-plane component is positive.[24] Despite the hyperbolic response, one does not observe a drastic change in the response of the propagating polaritons (Figure 2c), mainly due to the dominant effect of the in-plane permittivity on the optical response of the propagating waves in the thin film. In summary, the in-plane (ϵr,$\|$) and out-of-plane (ϵr,$\perp$) permittivity reveal metallic behavior (negative real permittivity) below 1.8 eV and dielectric behavior (positive real permittivity) above this threshold. This transition defines two distinct optical regimes in CuS thin films: a metallic regime supporting confined plasmon polaritons below 1.8 eV and a dielectric regime supporting guided photonic modes above 1.8 eV. These regimes are fundamental to understanding the optical properties and potential applications of CuS in plasmonic and photonic technologies.

2.2. Detecting Plasmonic and Photonic Modes in 2D NCs

To evaluate the plasmonic and photonic modes in the CuS nanomaterials, we positioned 2D NCs on monolayer graphene membranes (**Figure 3**). This method effectively mitigates substrate-induced effects by minimizing mode mixing and redshift in plasmon resonances.[46,47] Notably, the CuS NC stacks with thicknesses ranging from 1.7 to 39 nm (t/λ mapping,[48] where λ is the mean free path of the inelastic scattering and t is the thickness) were used in our experiments maintained their pristine (non-oxidized) state (Figures S1 and S2, Supporting Information). The thickness of the CuS NC shown in Figure 3a is measured to be ≈4 nm (Figure 3b,c). Figure 3d shows a model mimicking the experimental structure.

In Figure 3e, f, we present the electron energy loss (EEL) spectra obtained from the center and edge of ≈4 nm-thick CuS disk. The EEL spectra show multiple resonances below 2 eV. Due to the energy resolution of 0.17 eV and the instrumental broadening, the identification of low-energy plasmonic modes in the experimental EEL spectra is impossible. However, the decomposition of the EEL spectra allows the identification of the energies of the plasmonic modes. Here, the decomposition is performed by fitting the EEL spectra to multiple Gaussians. Each Gaussian peak in the decomposed EEL spectra corresponds to a plasmon mode. Although the CuS has a hybrid metallic-semiconducting nature, its excitation efficiency is not as high as that of noble metals (e.g., Au, Ag) with higher electron density. Since the cross-section of dipolar modes is larger than that of high energy modes, the excitation efficiency of dipolar modes is higher. To elucidate these resonances, we performed EEL simulations using the finite element method (FEM), as shown in Figure 3g,h. Both experimental and simulated EEL spectra show congruent resonance peaks. Further analysis involved the extraction of spatially resolved experimental EEL maps and computationally obtained normalized electric field maps, showing the absolute values of the electric fields for the computed eigenmodes, at the energies identified from the EEL spectra in Figure 3e–h. Although EEL maps and simulated normalized electric field maps effectively demonstrate

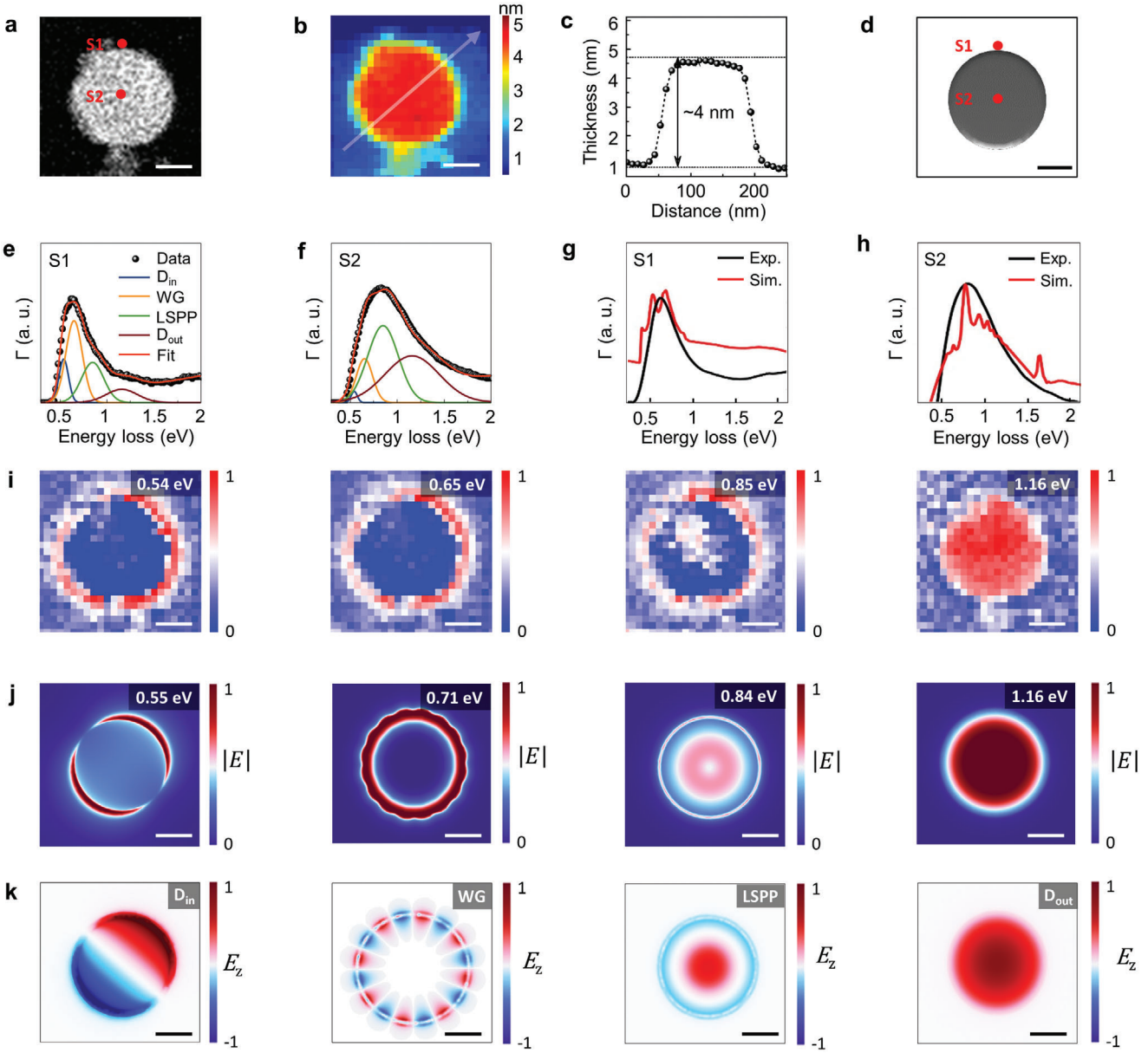

Figure 3. Plasmonic modes of CuS NCs on graphene. a) HAADF image of a CuS disk on graphene. b) Thickness mapping for the flake shown in (a). c) Line profile recorded on the semitransparent white line on the thickness mapping. d) A model corresponding to the experimental structure in (a). e,f) EEL spectra obtained at the marked positions on the HAADF image in (a). The spectra in (e,f) are deconvoluted by curve fitting. g,h) Comparison of experimental and simulated EEL spectra obtained at the positions marked in a and d. i,j) Spatially resolved EELS maps and simulated normalized electric field maps obtained at the energies identified from the EEL spectra in (e–h). k) Electric field distributions along z-axis are calculated at the energies that electric field maps generated. Scale bars are 50 nm (a,b,d,i,j,k).

the excitation of plasmon resonances below 2 eV, the accurate identification of these modes by EELS mapping is difficult.

To identify the nature of these plasmon resonances, we show the EELS maps, simulated normalized electric field maps as well as the electric field distributions along the z-axis in Figure 3i–k (the magnetic field distributions along the z-axis are shown in Figure S3, Supporting Information). Our results identify the 0.54 eV mode as an in-plane dipole (D_{in}) LSPR, alongside additional modes including a whispering-gallery (WG) mode at 0.65 eV, a Fabry-Pérot-like resonance or a localized surface plasmon polariton (LSPP) at 0.85 eV, where the plasmonic field is confined within the disk leading to an oscillation pattern along the radial direction, and another dipole mode in the z-direction (D_{out}) at 1.16 eV. The nature of the latter mode (dipolar out-of-plane) can be inferred from the pattern of the electric field components and the doughnut-like distribution of the magnetic field norm $|H|$ shown in Figure S4 (Supporting Information). In our simulations, we identified a number of other modes, shown in Figure S5 (Supporting Information), which are not visible in the EELS signal. Several reasons may explain this discrepancy.

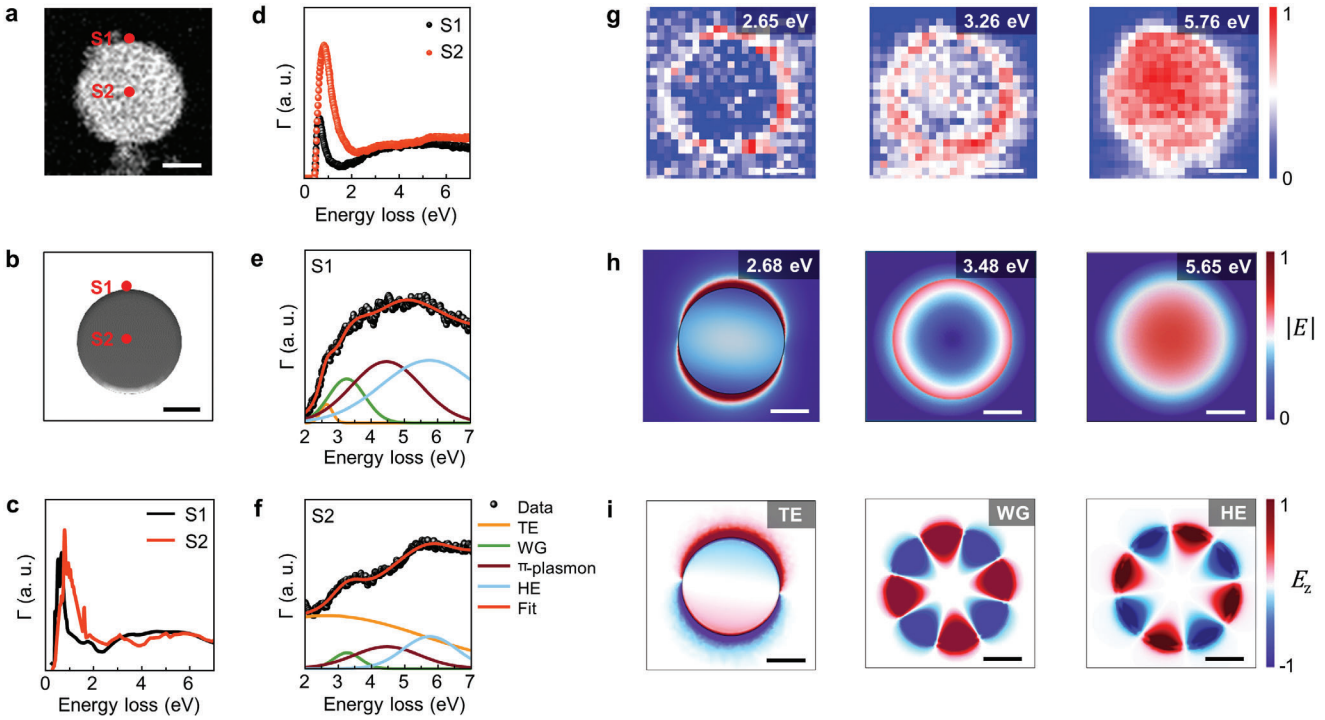

Figure 4. Photonic modes of CuS flakes on graphene. a) HAADF image of the CuS disk on graphene. b) A model corresponding to the experimental structure in (a). c,d) EEL spectra acquired at the marked positions in the HAADF image in a and the model in (b). e,f) Curve-fitting deconvoluted EEL spectra. g,h) Spatially resolved EELS maps and simulated normalized electric field maps obtained at energies identified from the EEL spectra in (c–f). i) Electric field distributions along z-axis are computed at the energies generated by the electric field maps. Scale bars are 50 nm (a,b,g,h,i).

Although EELS is a powerful method capable of detecting a wide range of plasmon modes, its effectiveness depends on factors such as the nature of the plasmon modes, the interacting geometry, and the aforementioned energy resolution.[49–51] For example, the LSPRs with very high damping or loss may not produce distinct peaks in the EEL spectrum. In addition, the plasmon modes with components that do not couple well with the electric field of the incident electron beam may be less detectable. In addition, the energy resolution of the EELS setup also limits the ability to distinguish closely spaced plasmon modes. Since the LSPRs in CuS NPs are closely spaced and the energy resolution is 0.17 eV, we cannot detect all the LSPRs below 2 eV in the experiment.

In addition to the CuS disks, we have also demonstrated the plasmonic nature of the CuS triangles (truncated triangular prism) (Figure S6, Supporting Information). As shown for the CuS disks, the truncated triangles also exhibit in-plane dipolar and edge LSPRs as well as an additional out-of-plane dipole mode below 2 eV. The electromagnetic confinement in CuS nanocrystals is strongly influenced by their geometry. The CuS triangles exhibit highly anisotropic field confinement, while disks display more isotropic modes but with weaker spatial confinement. In addition, we investigated the plasmonic nature of CuS NCs after annealing at 400 °C (Figure S7, Supporting Information). Interestingly, CuS disks subjected to annealing at 400 °C no longer exhibit LSPRs below 2 eV, suggesting changes in their plasmonic behavior. Changes in the plasmonic response are attributed to a phase transformation of covellite CuS to Cu-rich phases upon heating [52,53] and the disappearance of intense plasmon resonances in the NIR, which we observed in experiments at ambient conditions (Figure S8, Supporting Information).

Next, we investigated the photonic modes of the CuS nanocrystals using EELS analysis, as shown in **Figure 4**. EEL spectra acquired from the same CuS disk and the corresponding simulated EEL spectra reveal photonic modes excited at energies above 2 eV (Figure 4a–d). Using similar experimental protocols, we excited both the center and the edge of the CuS disk with a focused electron beam and acquired the EEL spectra from these regions (Figure 4a–f). In particular, the energy loss at 4.46 eV is attributed to the π-plasmon of graphene, as shown in Figure S9 (Supporting Information). Subsequent comparison of the experimental and simulated EEL spectrum revealed multiple excitations above 2 eV (Figure 4c,d).

To identify the photonic modes within the CuS disk, we analyzed EELS maps and simulated normalized electric field maps in Figure 4g,h. Both maps show similar patterns at the energies identified from the EEL spectra in Figure 4c–f. The electric and magnetic field distributions along the z-axis (Figure 4i; Figure S10, Supporting Information) clarify the photonic transverse electric (TE) mode, the photonic WG mode, and the hybrid WG (HE) photonic mode within the CuS disk. The HE mode has a hybrid nature with both magnetic and electric field z-components having similar profiles and a strong contribution due to retardation, while the WG resonance at an energy of 3.48 eV exhibits a uniform z-component of the magnetic field within the disc. In contrast to the plasmonic modes, the photonic modes of CuS nanocrystals remain unaffected after annealing at 400 °C (Figure S11, Supporting Information).

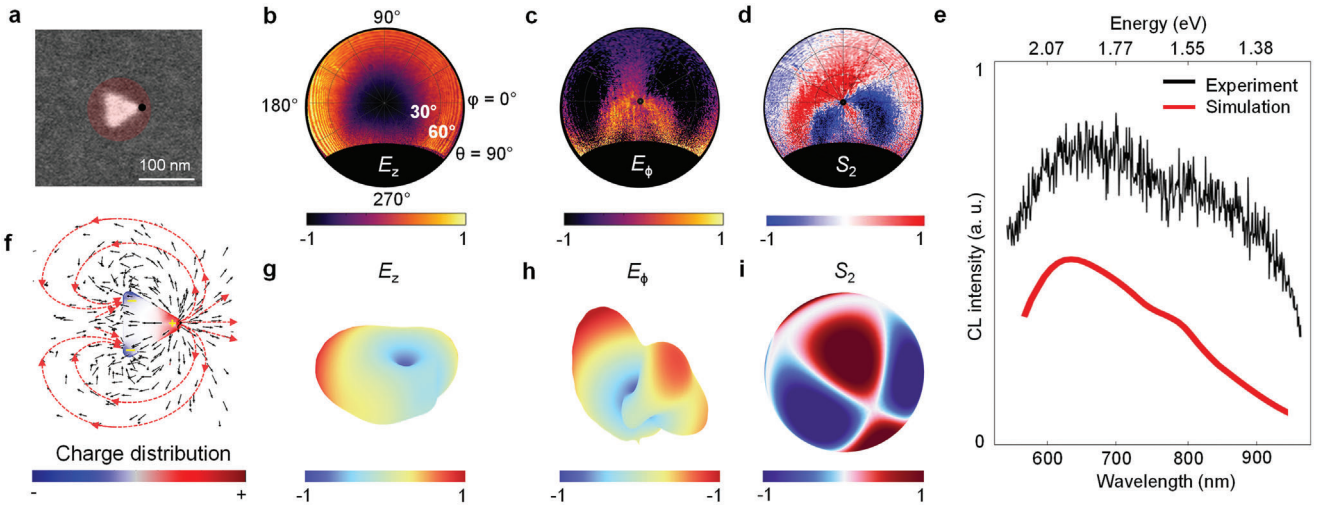

Figure 5. Light emission from electron-beam irradiated CuS NCs. a) SEM image of a CuS triangle. The electron beam is located at the position marked by a black dot in the CL measurements. b–d) E_z, E_ϕ and S_2 components captured by hyperspectral CL imaging, respectively. e) Experimental and simulated CL spectra obtained from a CuS triangle excited from its tip. f) Simulated surface charge distribution obtained at 1.6 eV. The arrows indicate the field vectors. g,h) Simulated far-field pattern of E_z and E_ϕ. i Simulated S_2 Stokes parameter.

The plasmonic and photonic properties of confined structures are highly dependent on their geometry. In CuS NCs with similar lateral sizes, increasing the sample thickness results in a blueshift in the energies of plasmonic modes, including D_{in}, WG, LSPP, and D_{out} (Figure S11, Supporting Information). However, the energy shift becomes less pronounced when the thickness exceeds ≈6 nm. Similarly, photonic modes in CuS NCs also exhibit a blueshift with increasing thickness (Figure S12, Supporting Information). Notably, while the TE mode's energy shift saturates at thicknesses greater than ≈3 nm, the energies of WG and HE photonic modes show an exponential increase with increasing thickness. In contrast to the effects of thickness, previous studies have demonstrated that an increase in the lateral flake size induces a redshift in the plasmon energies of CuS NCs.[17,24] This highlights the distinct roles of thickness and lateral size in modulating the optical properties of CuS nanostructures.

2.3. Visible and NIR Light Emission from Electron-Beam Irradiated CuS NCs

The radiative and non-radiative decay of photonic modes is modulated by changing the photonic mode density (PMD).[54,55] Far-field light emission is established by radiative decay of plasmonic or photonic modes in CuS NCs. Here, we perform CL measurements to verify the light emission of the CuS NCs (**Figure 5**). The SEM image in Figure 5a shows one of the triangular CuS NCs. CLS and polarimetry, combined with far-field simulation using the finite element method (FEM), are used to determine the electric field along the z-axis (E_z), the azimuthal component of the electric field (E_φ), and the S_2 Stokes parameter (Figure 5b–d). The CL spectra obtained from the CuS triangle excited from its tip show two distinct peaks at ≈1.55 and ≈1.94 eV (Figure 5e). The simulated CL spectra are in good agreement with the experimental data. The slight differences in the emission energies in the experimental and simulated CL data are due to the variations in the dimensions of the experimental structure. These results suggest that CuS NCs emit in the visible and NIR regions of the electromagnetic spectrum.

Based on the charge distribution and the components of E_φ and E_z, the dominant excited mode in the CuS triangle is likely to be the dipolar mode (Figure 5f) with mixed (plasmonic and photonic) character. The higher-energy peak (1.94 eV) is obviously due to a photonic mode as it shows higher intensity in the spectrum (less damping) while the lower energy peak (1.55 eV) is attributed to the plasmonic mode. It should be noted that the dipolar radiation cross-section is the dominant component in the far-field. Therefore, although EELS reveals the existence of higher-order resonances, the radiation efficiency of the higher-order resonances decreases significantly in intensity, making the dipole contribution the dominant radiation pattern in CL. This conclusion is drawn from several observations: i. The charge distribution shows a distinct dipole pattern, with regions of positive and negative charges separated across the triangle. This is characteristic of a dipolar mode, where charges oscillate between two opposite poles. ii. The E_z component in both the hyperspectral CL image and the simulated far-field pattern shows a strong central peak with a symmetric distribution. This is typical of a dipolar mode, where the electric field is concentrated along the polarization axis. iii. The E_φ component shows a lobed structure, indicating an angular variation that supports the dipole-like oscillation in the plane of the triangle. iv. The S_2 parameter, derived from the far-field electric field components, shows regions of alternating positive and negative values. This pattern is consistent with the expected distribution for a dipole mode.

3. Conclusion

In summary, we have investigated the plasmonic and photonic properties of individual CuS NCs with high energy resolution using a monochromated EELS in combination with cathodoluminescence spectroscopy. For the first time, we present

experimental evidence for shape-dependent NIR EM-field localization in NCs and confirm the ability of the metallic nature of the studied material to host a variety of plasmonic modes in this spectral region. Furthermore, we demonstrate the outcoupling of Vis-NIR light in the 600–900 nm range to the far field by the CuS NCs due to the in-plane dipolar resonances. In addition, a number of photonic modes in the visible and ultraviolet range have been demonstrated by EELS in individual colloidal CuS NCs for the first time. The non-plasmonic nature of these features was confirmed by EELS mapping of samples with different thermal pre-treatments and by simulations of electromagnetic field maps. These findings open the possibility of confining nanoscale polaritons in the covellite phase of copper sulfide over a broad spectral range.

4. Experimental Section

Material Synthesis: CuS NCs were synthesized according to procedures described elsewhere.[17,43] Briefly, 0.1 mmol of CuI was mixed with oleylamine (70% grade, Sigma-Aldrich) in a 50 mL three-necked flask in a Schlenk-line setup, stirred vigorously, degassed, transferred to a nitrogen atmosphere, and heated up. Later, 2 mL of sulfur/oleylamine solution (0.5 M), degassed and purged with nitrogen, was injected at 120 °C. After 10 min of synthesis, the reaction solution was cooled down to room temperature by injecting cold toluene into the flask. The nanodisks were prepared by reducing the synthesis time to 5 min. Nanotriangles were prepared by changing the Cu:S ratio to 1:20 and prompt quenching of the reaction by a cold bath. Hexagons were prepared by the main route described in the experimental section. All details of the synthesis of differently shaped CuS covellite NCs can be found in ref. [17] NCs were precipitated by adding a methanol/acetone mixture (1:1 vv) followed by centrifugation. The supernatant was discarded, the precipitate was diluted in hexane and the procedure was repeated.

Transfer of CuS NCs on Graphene: Prior to the transfer of CuS nanocrystals, CVD-grown monolayer graphene was attached to the TEM grids with a holey support film (quantifoil). First, a 10 nm Pt layer was deposited on the quantifoil of the TEM grid. Then, an Au TEM grid was precisely positioned onto the surface of the graphene, grown by chemical vapor deposition (CVD) on a Cu foil purchased from Graphenea Inc. A drop of isopropanol was then used to establish adhesion between the flake and the quantifoil of the TEM grid. The Cu foil was then dissolved with an ammonium persulfate solution (10%), resulting in the free-standing monolayer graphene membrane on the TEM grids. To eliminate any residual hydrocarbon contamination on the graphene surface, the TEM grids were annealed at 300 °C for 15 min. Finally, CuS nanocrystals dispersed in hexane were subjected to a sonication process for 2 h before being drop-cast onto the graphene membrane attached to the TEM grid.

TEM and HRTEM Measurements: The basic characterization of NCs was performed on a Talos–L120C TEM with a thermal emitter operated at an acceleration voltage of 120 kV. Samples were prepared by diluting the batch solution of NCs with toluene and drop-casting 10 µL of the solution onto a copper grid coated with a carbon film.

HRTEM Image Simulations: HRTEM image simulations were performed using QSTEM software.[56] The following parameters were used in the HRTEM simulations: a spherical aberration coefficient of 1 µm, acceleration voltage of 120 kV, and defocus of 2.5 nm. The crystal structure of CuS used in the image simulations was obtained from the American Mineralogist Crystal Structure Database (database code: amcsd 0000065).

PXRD Measurement: X-ray powder diffraction measurements were performed on a Panalytical Aeris diffractometer using reflection (Bragg-Brentano) geometry. The instrument was equipped with a copper anode with an X-ray wavelength of 1.5406 Å from the Cu-Kα1 line. NCs were drop-casted from the batch solution onto a low background silicon substrate and measured in the dried state.

Optical Measurements: UV–vis absorption spectra were recorded using a PerkinElmer Lambda 1050+ spectrophotometer equipped with an integrating sphere. NCs batch solution was diluted with toluene or transferred to TCE and placed in 10 mm optical length quartz cuvettes from Hellma Analytics.

EELS and EDS Measurements: STEM and EELS measurements were performed with the sub-electron-volt-sub-angstrom microscope (Zeiss SESAM). This microscope includes a Schottky field-emission gun, an OMEGA-type electrostatic monochromator, and the MANDOLINE filter, allowing experiments with an energy resolution of ≈0.1 eV. The microscope was operated with an acceleration voltage of 200 kV, an energy resolution of 0.17 eV, an energy dispersion of 0.015 eV px^{-1}, and an EELS collection semi-angle of 0.7 mrad. EELS maps were acquired with a pixel dwell time of 0.5 s and integrated over an energy window of 0.2 eV. After data acquisition, our analytical approach included a multivariate weighted principal component analysis (PCA) routine.[57] For energy dispersive X-ray spectroscopy (EDS) measurements, a JEOL ARM200F FEG-STEM/TEM instrument, equipped with a cold field-emission gun, a post-specimen spherical aberration corrector (Cs), and a Gatan GIF Quantum ERS electron energy loss spectrometer, was used. EDS experiments were performed under identical conditions with an acceleration voltage of 80 kV. First, EELS maps were acquired, which provided 4D data, on CuS NCs. For each CuS NC, EELS spectrum images were recorded, which consist of spatially resolved EELS data collected pixel by pixel over the particle. Then specific areas on the spectrum image of CuS NCs were selected and the EEL spectra were deduced. From the EELS data, spectra corresponding to the center and edge of the NCs were extracted by selecting specific regions of interest on the spectrum image. The exact placement of these regions was guided by the high spatial resolution of the spectrum image, ensuring accurate localization of the EEL signals.

CL Measurements: For CLS and polarization studies, a Zeiss SIGMA optical field emission microscope equipped with a CL compartment provided by Delmic B.V was used. A focused electron beam with an acceleration voltage of 30 kV and a beam current of 9 nA was used to scan the sample and excite its surface. The radiated light was collected by an off-axis aluminum parabolic mirror positioned above the sample. This mirror had a focal length of 0.5 mm and an acceptance angle of 1.46π sr. The exposure time was set to 30 s. The collected light was directed to a detector and an additional polarizer module was used to generate angle-resolved maps and to determine the Stokes parameters, respectively.

CL and EELS Simulations: Numerical simulations of CL emission and electron energy-loss spectra were performed using the COMSOL Multiphysics software package with its Radiofrequency (RF) Toolbox. Maxwell's equations were solved in the frequency domain by using the finite-element method and in real space in a 3D simulation domain, based on the experimentally determined geometries of the structures. To simulate the electron beam, an oscillating "edge current" along a straight line was used as the source of the electromagnetic field in the system. The current is expressed by $I = I_0 \exp(i\omega z/v_e)$, where v_e is the velocity of the moving electron along the z-axis. CL spectra were obtained by integrating the Poynting vector of the three coordination components of the emitted light over the entire top surface of the simulation domain. The electron energy loss (EELS) probability Γ of an electron losing energy $\hbar\omega$ is calculated from the integration of the induced electric field along the entire electron trajectory.[58] For the S_2 parameter, the transverse components of the electric field and their vector distribution at each spatial point were used. In this calculation, the formula $S_2 = (E_{\parallel}E_{\perp}^{*} + E_{\perp}E_{\parallel}^{*})$ was applied at the far-field components of the electric field projected on the upper and lower hemispheres.[42]

Supporting Information

Supporting Information is available from the Wiley Online Library or from the author.

Acknowledgements

R.L., S.S., U.P. acknowledge the support of the Collaborative Research Center SFB 1477 "Light-Matter Interactions at Interfaces (LiMatI)", project

number 441234705 (Deutsche Forschungsgemeinschaft). C. K. acknowledges the European Regional Development Fund of the European Union for the funding of the PL spectrometer (GHS-20-0035/P000376218), the X-ray diffractometer (GHS-20-0036/P000379642) and the Deutsche Forschungsgemeinschaft (DFG) for the funding of a ThermoFisher Talos L120C electron microscope (INST 264/188-1 FUGG). NT acknowledges funding from the European Research Council (ERC) under the European Union's Horizon 2020 The Research and Innovation Programme under grant agreement no. 802130 (Kiel, NanoBeam), 101157312 (Kiel, UltraCoherentCL), and grant agreement no. 101017720 (EBEAM), and from the Deutsche Forschungsgemeinschaft under Grant Agreement No. 525347396 and 447330010, and from the Volkswagen Foundation (Momentum Grant).

Open access funding enabled and organized by Projekt DEAL.

Conflict of Interest

The authors declare no conflict of interest.

Data Availability Statement

The data that support the findings of this study are available from the corresponding author upon reasonable request.

Keywords

cathodoluminescence, copper sulfide, covellite, EELS mapping, nanocrystal, photonic mode, plasmonic mode

Received: November 29, 2024
Revised: December 10, 2024
Published online: December 26, 2024

[1] Z. Hu, R. O'Neill, R. Lesyuk, C. Klinke, *Acc. Chem. Res.* **2021**, *54*, 3792.
[2] J. Feldmann, G. Peter, E. O. Göbel, P. Dawson, K. Moore, C. Foxon, R. J. Elliott, *Phys. Rev. Lett.* **1987**, *59*, 2337.
[3] S. Ithurria, M. D. Tessier, B. Mahler, R. Lobo, B. Dubertret, A. L. Efros, *Nat. Mater.* **2011**, *10*, 936.
[4] N. Talebi, S. Meuret, S. Guo, M. Hentschel, A. Polman, H. Giessen, P. A. van Aken, *Nat. Commun.* **2019**, *10*, 599.
[5] N. Talebi, *Phys. Rev. Lett.* **2020**, *125*, 80401.
[6] M. Taleb, F. Davoodi, F. K. Diekmann, K. Rossnagel, N. Talebi, *Adv. Photonics Res.* **2022**, *3*, 2100124.
[7] F. Davoodi, M. Taleb, F. K. Diekmann, T. Coenen, K. Rossnagel, N. Talebi, *ACS Photonics* **2022**, *9*, 2473.
[8] J. Chen, M. Badioli, P. Alonso-González, S. Thongrattanasiri, F. Huth, J. Osmond, M. Spasenović, A. Centeno, A. Pesquera, P. Godignon, *Nature* **2012**, *487*, 77.
[9] A. N. Grigorenko, M. Polini, K. S. Novoselov, *Nat. Photonics* **2012**, *6*, 749.
[10] X. Luo, T. Qiu, W. Lu, Z. Ni, *Materials Science and Engineering: R: Reports* **2013**, *74*, 351.
[11] S. Xiao, X. Zhu, B.-H. Li, N. A. Mortensen, *Front. Phys.* **2016**, *11*, 1.
[12] C. Lian, S.-Q. Hu, J. Zhang, C. Cheng, Z. Yuan, S. Gao, S. I. Meng, *Phys. Rev. Lett.* **2020**, *125*, 116802.
[13] Y. Abdi, M. Taleb, S. Hajibaba, M. Moayedi, N. Talebi, *arXiv* **2024**, *2404*, 13609.
[14] M. Su, Z. Wu, T. Yan, N. Li, X. Li, T. Hou, J. Liu, C. Zhang, C. Zhu, Z. Wang, *Adv. Funct. Mater.* **2024**, *34*, 2409580.
[15] W. Xu, H. Liu, D. Zhou, X. Chen, N. Ding, H. Song, H. Ågren, *Nano Today* **2020**, *33*, 100892.
[16] N. Kapuria, N. N. Patil, K. M. Ryan, S. Singh, *Nanoscale* **2022**, *14*, 2885.
[17] R. Lesyuk, E. Klein, I. Yaremchuk, C. Klinke, *Nanoscale* **2018**, *10*, 20640.
[18] M. Sakamoto, M. Hada, W. Ota, F. Uesugi, T. Sato, *Nat. Commun.* **2023**, *14*, 4471.
[19] I. I. Mazin, *Physical Review B—Condensed Matter and Materials Physics* **2012**, *85*, 115133.
[20] S. Conejeros, I. d. P. Moreira, P. Alemany, E. Canadell, *Inorg. Chem.* **2014**, *53*, 12402.
[21] A. Morales-García, A. L. Soares Jr., E. C. Dos Santos, H. A. de Abreu, H. A. Abreu, H. A. Duarte, *The Journal of Physical Chemistry A* **2014**, *118*, 5823.
[22] L. Xiao, J. Wu, J. Ran, Y. Liu, W. Qiu, F. Lu, F. Shao, D. Tang, P. Peng, *AIP Adv.* **2016**, *6*.
[23] F. Di Benedetto, M. Borgheresi, A. Caneschi, G. Chastanet, C. Cipriani, D. Gatteschi, G. Pratesi, M. Romanelli, R. Sessoli, *Eur. J. Mineral.* **2006**, *18*, 283.
[24] R. M. Córdova-Castro, M. Casavola, M. van Schilfgaarde, A. V. Krasavin, M. A. Green, D. Richards, A. V. Zayats, *ACS Nano* **2019**, *13*, 6550.
[25] X. Han, X. Ma, Q. Miao, X. Zhang, D. He, X. Yu, Y. Wang, *ACS Omega* **2024**, *9*, 22248.
[26] Y. Yan, N. J. Spear, Q. Meng, M. R. Singh, J. E. Macdonald, R. F. Haglund, *Nano Lett.* **2024**, *24*, 5085.
[27] Y. Xie, A. Riedinger, M. Prato, A. Casu, A. Genovese, P. Guardia, S. Sottini, C. Sangregorio, K. Miszta, S. Ghosh, *J. Am. Chem. Soc.* **2013**, *135*, 17630.
[28] V. B. Llorente, V. M. Dzhagan, N. Gaponik, R. A. Iglesias, D. R. T. Zahn, V. Lesnyak, *J. Phys. Chem. C* **2017**, *121*, 18244.
[29] J. Nelayah, M. Kociak, O. Stéphan, G. Abajo, F. Javier, M. Tencé, L. Henrard, D. Taverna, I. Pastoriza-Santos, L. M. Liz-Marzán, C. Colliex, *Nat. Phys.* **2007**, *3*, 348.
[30] F. Roth, A. König, J. Fink, B. Büchner, M. Knupfer, *J. Electron Spectrosc. Relat. Phenom.* **2014**, *195*, 85.
[31] C. Colliex, M. Kociak, O. Stéphan, *Ultramicroscopy* **2016**, *162*, A1.
[32] A. L. Koh, K. Bao, I. Khan, W. E. Smith, G. Kothleitner, P. Nordlander, S. A. Maier, D. W. McComb, *ACS Nano* **2009**, *3*, 3015.
[33] B. Ögüt, N. Talebi, R. Vogelgesang, W. Sigle, P. A. van Aken, *Nano Lett.* **2012**, *12*, 5239.
[34] S. Guo, N. Talebi, P. A. van Aken, *ACS Photonics* **2018**, *5*, 1326.
[35] N. Talebi, W. Sigle, R. Vogelgesang, M. Esmann, S. F. Becker, C. Lienau, P. A. van Aken, *ACS Nano* **2015**, *9*, 7641.
[36] B. Schröder, T. Weber, S. V. Yalunin, T. Kiel, C. Matyssek, M. Sivis, S. Schäfer, F. Cube, S. Irsen, K. Busch, *Phys. Rev. B* **2015**, *92*, 85411.
[37] N. W. Bigelow, A. Vaschillo, J. P. Camden, D. J. Masiello, *ACS Nano* **2013**, *7*, 4511.
[38] O. Nicoletti, M. Wubs, N. A. Mortensen, W. Sigle, P. A. van Aken, P. A. Midgley, *Opt. Express* **2011**, *19*, 15371.
[39] F. G. Abajo, *Rev. Mod. Phys.* **2010**, *82*, 209.
[40] F. G. Abajo, M. Kociak, *Phys. Rev. Lett.* **2008**, *100*, 106804.
[41] T. Coenen, E. J. R. Vesseur, A. Polman, *Appl. Phys. Lett.* **2011**, *99*, 143103.
[42] R. Lingstädt, F. Davoodi, K. Elibol, M. Taleb, H. Kwon, P. Fischer, N. Talebi, P. A. van Aken, *ACS Nano* **2023**, *17*, 25496.
[43] X.-J. Wu, X. Huang, X. Qi, H. Li, B. Li, H. Zhang, *Angew. Chem., Int. Ed.* **2014**, *53*, 8929.
[44] D. Baranov, M. J. Lynch, A. C. Curtis, A. R. Carollo, C. R. Douglass, A. M. Mateo-Tejada, D. M. Jonas, *Chem. Mater.* **2019**, *31*, 1223.
[45] M. Ohmasa, M. Suzuki, Y. Takéuchi, *CuS. Mineralogical Journal* **1977**, *8*, 311.
[46] K. Elibol, P. A. van Aken, *Nano Lett.* **2022**, *22*, 5825.
[47] K. Elibol, P. A. van Aken, *ACS Nano* **2022**, *16*, 11931.
[48] T. Malis, S. C. Cheng, R. F. Egerton, *Journal of electron microscopy technique* **1988**, *8*, 193.

[49] M. Bosman, E. Ye, S. F. Tan, C. A. Nijhuis, J. K. W. Yang, R. Marty, A. Mlayah, A. Arbouet, C. Girard, M.-Y. Han, *Sci. Rep.* **2013**, *3*, 1312.
[50] E. P. Bellido, D. Rossouw, G. A. Botton, *Microsc. Microanal.* **2014**, *20*, 767.
[51] A. Agrawal, I. Kriegel, D. J. Milliron, *J. Phys. Chem. C* **2015**, *119*, 6227.
[52] E. N. Selivanov, R. I. Gulyaeva, A. D. Vershinin, *Inorg. Mater.* **2007**, *43*, 573.
[53] M. T. S. Nair, L. Guerrero, P. K. Nair, *Semicond. Sci. Technol.* **1998**, *13*, 1164.
[54] W. L. Barnes, *J. Mod. Opt.* **1998**, *45*, 661.
[55] X. Fu, C. Peng, M. Samal, N. Barange, Y.-A. Chen, D.-H. Shin, Y. Mehta, A. Rozelle, C.-H. Chang, F. So, *ACS Appl. Electron. Mater.* **2020**, *2*, 1759.
[56] C. T. Koch, *Determination of core structure periodicity and point defect density along dislocations*, Arizona State University, 1151 S Forest Ave, USA **2002**.
[57] M. Bosman, M. Watanabe, D. T. L. Alexander, V. J. Keast, *Ultramicroscopy* **2006**, *106*, 1024.
[58] F. Davoodi, N. Talebi, *ACS Appl. Nano Mater.* **2021**, *4*, 6067.